Phonon Interaction with Ripples and Defects in Thin Layered Molybdenum Disulfide

Brandon Smith,[1] Lucas Lindsay,[2] Jaehyun Kim,[1] Eric Ou,[1] Rui Huang,[3] Li Shi[1,a)]

Affiliations

[1]Department of Mechanical Engineering, The University of Texas at Austin, Austin, TX 78712, USA

[2]Materials Science and Technology Division, Oak Ridge National Laboratory, Oak Ridge, TN 37831, USA

[3]Department of Aerospace Engineering and Engineering Mechanics, The University of Texas at Austin, Austin, TX 78712, USA

[a)]lishi@mail.utexas.edu

Abstract

Compared to other extrinsic phonon scattering mechanisms such as surface and interior defects, phonon scattering and lattice thermal resistance due to structural rippling in few-layer two-dimensional (2D) materials is under-examined. Here the temperature-dependent basal-plane thermal conductivities (κ) of one rippled and four flat molybdenum disulfide (MoS_2) samples are measured with a four-probe thermal transport measurement method. A flat 18 nm thick sample and a rippled 20 nm thick sample show similar peak κ values of 122±17 and 129±19 W m^{-1} K^{-1}, respectively. In comparison, a 32 nm thick flat sample has a peak κ of only 58±11 W m^{-1} K^{-1} despite having increased thickness. The peak thermal conductivities of the five samples decrease with increasing integrated Raman intensity caused by defects in the frequency range of the phonon band gap in MoS_2. In conjunction with the experimental

findings, theoretical calculations of the temperature-, thickness-, strain-, and defect-dependent κ of thin MoS_2 layers reveal the importance of interior defect scattering over scattering from compression-induced ripples and surface defects in these samples. The results further clarify the conditions where ripples are important in determining the basal plane thermal resistance in layered systems.

Main Text

Due to thermal fluctuations,[1] structural rippling is ubiquitous in monolayer and few-layer two-dimensional (2D) materials, including both supported[2,3] and suspended[4–8] structures, such as molybdenum disulfide (MoS_2) and graphene. This rippling creates inhomogeneous strain fields due to the changed crystal structure that strongly affect electronic and vibrational behaviors. For example, severe rippling in graphene was shown to generate a long-range scattering potential for electrons and strongly suppress their weak localization.[9–11] In addition, the effects of ripples and kinks on thermal conductivity (κ) in 2D materials has been considered in several theoretical studies, including unique strain effects,[12–18] which can influence the performance and thermomechanical reliability of emerging 2D devices.[19–21] Contrary to bulk materials for which compressive and tensile strains generally increase and decrease the thermal conductivity,[14] respectively, molecular dynamics studies have suggested that both tensile and compressive strains reduce the thermal conductivities of graphene and MoS_2.[12,14,15,17] In particular, compressive strain in 2D layers tends to drive the formation of buckling and rippling of the structure to relax the induced strain. Although a few theoretical studies have proposed that buckling or rippling due to compressive strains can increase phonon scattering rates, and thus reduce the thermal conductivity of 2D layers,[14,17] it has also been suggested that the basal plane thermal conductivity of 2D layers is rather robust against rippling.[15] Thus, the conditions and criteria for the importance of compression-induced ripple effects on thermal transport in 2D materials remains unclear.

Here, we report four-probe thermal transport measurements of the intrinsic basal plane thermal conductivities of both rippled and flat multilayer molybdenum disulfide (MoS_2) samples, which are representative of 2D layered materials in general. Our experiments demonstrate that the basal plane thermal conductivity is robust against compression-induced ripples and kinks with radius of curvatures on the micrometer scale, but sensitive to phonon-defect scattering. A clear correlation is drawn between the peak thermal conductivity and the integrated Raman intensity caused by defects in the frequency range of the phonon band gap in MoS_2. In conjunction with experiments, first principles calculations of temperature, thickness, strain, and point defect concentration dependent κ provide physical insights into phonon-defect interactions and thermal resistance, and thus clarify the conditions for which ripples become an important mechanism for thermal conductivity suppression.

Multilayer MoS_2 samples were exfoliated from natural MoS_2 crystals that were used in a previous two-probe thermal transport measurement of few-layer MoS_2.[22] The exfoliation and dry transfer method for the MoS_2 samples was similar to the process reported for four-probe thermal transport measurements of multilayer black phosphorus samples.[23] The thickness is uniform on each sample chosen for the transfer based on the absence of color variation in the thin sample on the exfoliated substrate, where the color variation across even a monolayer step is detectable. The one rippled and four flat samples examined by the four-probe microdevice shown in Figure 1(a) are between 18 nm and 57 nm thick, a range where intrinsic rippling due to thermal fluctuations is negligible and the existence of rippling is solely induced by compressive strain. Figures 1(b) and 1(c) show the center suspended segments of the rippled sample and another flat sample, respectively. Based on the different heat flow rates through the contact points and in the sample, this unique four-probe thermal transport microdevice simultaneously measures the intrinsic thermal resistance (R_2) of the center suspended segment of the sample as well as the contact thermal resistance with the two inner resistance thermometers ($R_{c,2}$ and $R_{c,3}$).[23–25]

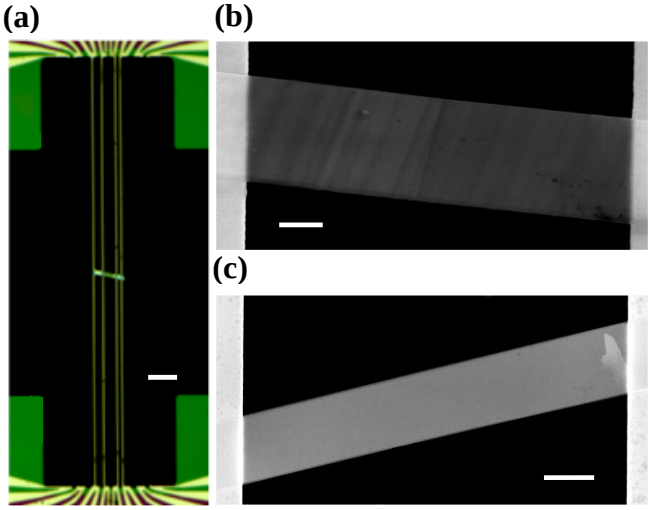

FIG. 1. Four-probe microdevice with rippled and flat MoS_2 samples. (a) Optical micrograph of a 20 nm thick, 3.4 μm wide rippled MoS_2 sample suspended on a four-probe thermal measurement device that consists of four suspended Pd/Cr/SiN_x beams. The scale bar is 20 μm. (b, c) Scanning electron microscopy (SEM) images of the center suspended segments of (b) the 20 nm thick rippled sample and (c) a 57 nm thick flat sample. The scale bars are 1 μm and 2 μm for (b) and (c), respectively.

Upon completion of the transport measurements, atomic force microscopy (AFM) was used to probe the surface topography of the 20 nm rippled sample directly on the suspended device, as seen in Figure 2. For this AFM profile, a third-order plane fit is used to show the ripples clearly by removing the curvature due to a sag of the suspended sample segment, as shown in Figure S3 of the Supplementary Material. Sagging of the multilayer material can lead to compression of the top layers and tension in the bottom layers. With relatively weak van der Waals interactions between the layers, rippling of the top layers relaxes the compressive strain, as illustrated in the schematic of Figure 2. A similar ripple morphology

has been observed in multiwalled carbon nanotubes under bending and predicted for multilayer graphene under compression.[26–29] Previous studies have demonstrated 6–10 nm wavelength and 0.6–1 nm amplitude for ripples in suspended monolayer MoS_2 samples, and 40–300 nm wavelength and 1–25 nm amplitude for ripples in supported monolayer MoS_2 samples.[3,8] In comparison, the average wavelength (λ) and amplitude (A) of the ripples in the 20 nm sample are 0.67 μm and 7.4 nm, respectively, with radius of curvatures in the range between 1 and 7 μm. In addition, a kink is present at the midpoint of the center suspended segment at a depth of 580 nm below the plane of the supporting thermometer lines, as depicted in Figure S3, and exhibits a radius of curvature of 0.67 μm. The strain is calculated by comparing the top surface contour length from AFM data and the lengths of a smooth 2nd order polynomial fit to the left and right sides of the kink. Assuming the ripples fully relax the compressive strain in the top layer, the contour length (8.38 μm) is unstrained and the smooth polynomial fit yields the compressed length (8.36 μm) without rippling. Hence, the relative difference between the two lengths gives a compressive strain of 0.14% if the strain were not relaxed by rippling. The tensile strain in the bottom layer is approximately the same in magnitude as the compressive strain value assuming the neutral plane remains close to the middle layer.

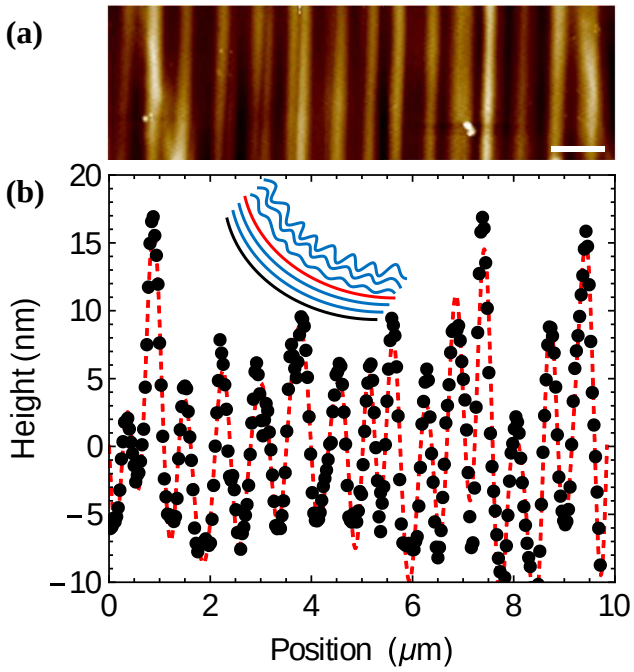

FIG. 2. Rippled sample surface morphology. (a) Atomic force microscopy (AFM) height image of the center suspended segment of the 20 nm thick rippled sample. The scale bar is 1 μm. (b) The measured AFM height (black dots) as a function of the sample position for a typical individual scan line. The red dashed fitting curve aids the visualization of the ripples. The inset illustrates the proposed layer morphology of the ripples that relax the compressive strain.

The contact thermal resistances measured for the MoS_2 samples here are appreciable only at temperatures below 150 K, as shown in Figure S4. The intrinsic thermal conductivities depicted in Figure 3 of the one rippled and four flat MoS_2 samples are calculated from the thermal resistance, R_2, of the center suspended segment and the measured sample dimensions. The measured peak thermal conductivities of the 20 nm rippled sample and the 18 nm flat sample are comparable, 129±19 and 122±17 W m^{-1} K^{-1}, respectively, at temperatures near 85 K. Thus, the rippling observed in the 20 nm sample appears to yield negligible impact on phonon transport. In comparison, the peak thermal conductivity for a 32 nm flat MoS_2 sample is 58±11 W m^{-1} K^{-1} at 87 K, considerably lower than the corresponding values for three other

samples, including the rippled 20 nm sample, flat 18 nm sample, and 28 nm flat sample that has a peak thermal conductivity of 94±14 W m^{-1} K^{-1}. Additionally, the largest peak thermal conductivity of 151±5 W m^{-1} K^{-1} is found in the thickest 57 nm flat sample measured.

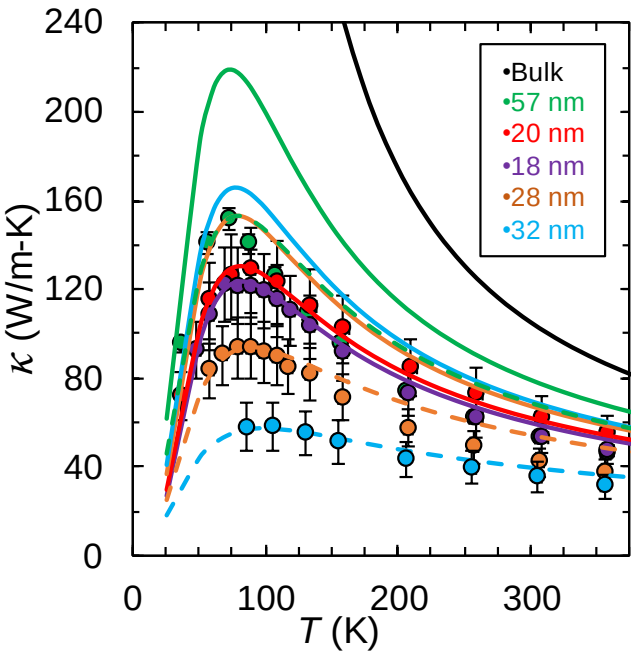

FIG. 3. Temperature-dependent basal plane thermal conductivities of MoS_2 flakes. The filled circles are measurement results for samples of varying thickness as indicated in the legend. The solid curves are calculations for defect-free samples at the thickness corresponding to the color of the circle symbols. The dashed curves are calculations with additional phonon scattering by Mo vacancies at concentrations of 2 x10^{19} cm^{-3}, 3.75 x10^{19} cm^{-3}, and 1.5 x10^{20} cm^{-3} for the 57 nm, 28 nm, and 32 nm thick samples, respectively. The error bars on the measured data are determined from Monte Carlo error propagation of the random and systematic errors in the thermal resistance measurements and account for dimensional and sample angle uncertainties.

To understand the measurement results, Raman spectroscopy was utilized to indirectly probe point defects in the samples. Based on the calculated phonon dispersion of MoS_2, the

phonon density of states (pDOS) vanishes in the frequency range between 245.5 to 288.75 cm^{-1}, as shown in Figure 4(a). The background intensity measured by Raman spectroscopy in this frequency range is caused by interaction with localized electronic and vibrational defect states.[30] Figure 4(b) demonstrates that the measured peak thermal conductivities of the five samples normalized by the corresponding theoretical defect-free peak thermal conductivities generally decrease with increasing integrated Raman background intensity in the zero pDOS region. A similar correlation between the reduced thermal conductivity and large integrated Raman intensity was recently observed in boron arsenide samples.[31] These results reveal the importance of point defect scattering in high-thermal conductivity materials. The variation in the point defect densities in the five MoS_2 samples should be traced to the source powder materials used for the exfoliation.

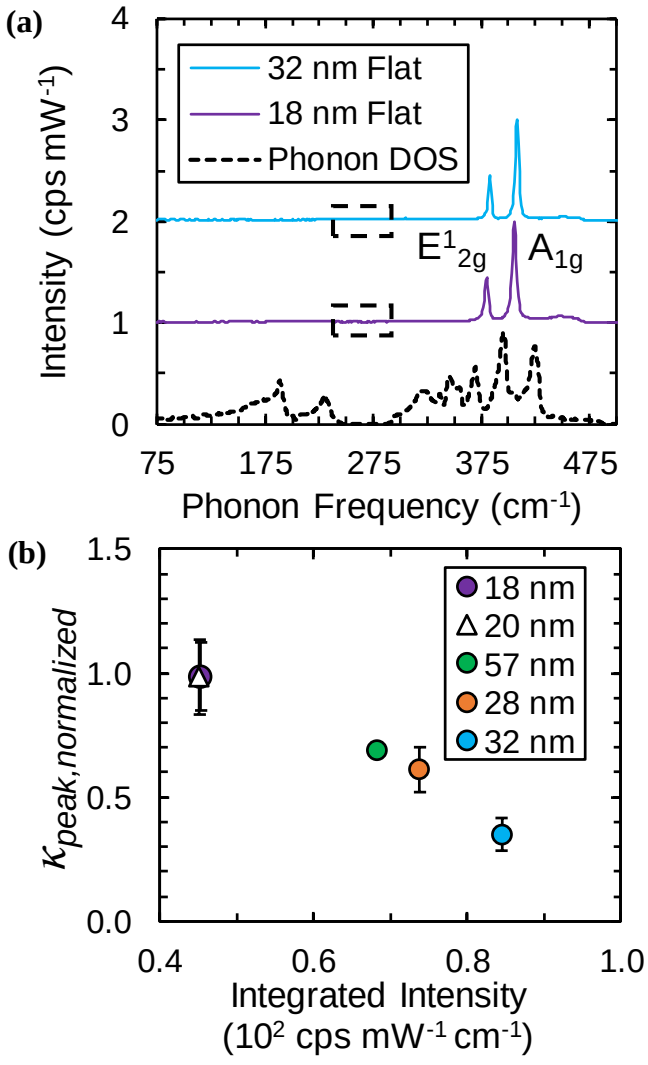

FIG. 4. Raman spectroscopy characterization. (a) Raman spectra of two representative MoS_2 samples along with the phonon density of states from first principles calculations. The black dashed rectangles indicate the phonon frequency range where the Raman background intensities were integrated. (b) Measured peak thermal conductivity normalized by the calculated theoretical defect-free peak value for each sample thickness as a function of the integrated Raman spectra intensity in the frequency range between 245.5 to 288.75 cm^{-1}.

To develop microscopic physical insights of the measurements, first principles phonon transport calculations were carried out, accounting for intrinsic three-phonon scattering[32,33], and extrinsic scattering by isotopes,[34] top and bottom surfaces, and Mo vacancies that are used here to represent point-defect scattering.[32] With these scattering terms as inputs, full solution of the Peierls-Boltzmann transport equation determines the transport phonon lifetimes that are critical for determining the thermal conductivity.[35–37] To evaluate the effect of phonon-point-defect scattering on thermal conductivity in the MoS_2 samples, Mo vacancies were introduced into the calculations as mass defects similar to phonon-isotope scattering, with the defect concentration as the single tuning parameter varied to fit the measured data of each sample. Scattering from force variance due to vacancies was not considered but is expected to give similar behavior for concentrations less than those determined here.[38–40] Furthermore, other point defect types are expected to give similar frequency dependence of the scattering rates and similar temperature dependent behavior of the thermal conductivity but will alter the concentrations needed to fit the experimental data. S vacancies were also examined, but they gave much weaker thermal resistance, at similar concentrations, than the Mo vacancies as the vibrations of the heavier Mo atoms govern the behavior of the heat-carrying acoustic modes.

Accounting for diffuse scattering by surface roughness, the calculated thermal conductivities for interior defect-free 18 nm and 20 nm samples agree reasonably with the

measured data over the entire temperature range, as shown in Figure 3. However, fitting the calculation results to the measured data for the 57 nm, 28 nm, and 32 nm flat samples requires significant concentrations of interior point defect vacancies, $2x10^{19}$, $3.75x10^{19}$, and $1.5x10^{20}$ cm^{-3}, respectively. The obtained point defect concentrations increase with increasing Raman background intensity values measured in the zero pDOS region shown in Figure 4(b). Comparison of the measured and calculated conductivity data suggests that phonon surface scattering is mostly diffuse and phonon scattering from point defects is important.

We next consider the effect of ripple geometry and strain on the lattice thermal conductivity. As shown in the Supplementary Material, the wavelength and mean free paths of the heat carrying phonons calculated via first principles are shorter than approximately 5 nm and 500 nm, respectively, which are smaller than the 1-7 μm radius of curvatures of the induced ripples and the 3.9 and 4.4 μm distance between the kink and either edge. This comparison suggests that the ripple geometry has a negligible effect on phonon scattering when the ripple geometry is much larger than the wavelengths and mean free paths of the heat-carrying phonons. Additionally, our first principles calculations demonstrate that the lattice thermal conductivity decreases with increasing biaxial tensile strain, as shown in Figure S7, in agreement with previous theoretical studies of 2D materials.[12,14,15,17,18] Under biaxial compressive strain, first principles calculations give imaginary phonon modes for bulk MoS_2 suggesting structural instability, likely due to the energetically favorable rippling geometry. While relaxation of the compressive strain in the top layer via the ripples of micrometer curvature results in negligible effect on the phonon dispersion and scattering, tensile strain at a level of ~0.14% in the bottom layers may reduce basal plane thermal conductivity by a few percent.[18]

In conclusion, the ripple geometry observed here has negligible effect on phonon scattering because the radius of curvatures of the compression-induced ripples in the 2D layers are on the micrometer scale and much larger than both the mean free paths and

wavelengths of heat-carrying phonons. In addition, the ripples relax the compressive strain in the top layers, while the tensile strains in the bottom layers are calculated to be insufficient to cause apparent suppression of the thermal conductivity. The ripple effect on the basal-plane thermal conductivity is expected to be important when the radius of curvature of compression-induced ripples in 2D layered materials decreases toward the mean free paths of heat-carrying phonons. On the other hand, phonon scattering by point defects, which were correlated with integrated Raman intensity in the MoS_2 phonon bandgap, is an important extrinsic phonon mechanism that determines the thermal conductivity in multilayer MoS_2 nanoflakes. Comparisons between measurements and first principles calculations also reveal an approximately diffuse nature of phonon scattering by the top and bottom surfaces of the exfoliated MoS_2 flakes due to the presence of surface defects. These findings clarify the extrinsic phonon scattering effects in emerging 2D functional materials.

Supplementary Material

See Supplementary Material for details of the device fabrication, measurement with the four-probe microdevice, sample characterization, Raman spectroscopy, and theoretical calculations.

Acknowledgements

We thank David Choi, Sean Sullivan, and Evan Fleming for assistance in AFM, Raman spectroscopy, and fast Fourier transform data analysis, respectively. The thermal transport measurements of four samples were completed with support from U.S. Office of Naval Research award N00014-16-1-2798. Thermal transport measurements of the fifth sample, all Raman measurements, and the manuscript preparation were completed with support from U.S. Department of Energy, Office of Science, Basic Energy Sciences award DE-FG02-07ER46377. The first principles calculations conducted by L. L. were supported by

the U. S. Department of Energy, Office of Science, Basic Energy Sciences, Materials Sciences and Engineering Division. We acknowledge use of Texas Nanofabrication Facilities supported by the NSF NNCI Award 1542159.

References

[1] A. Fasolino, J.H. Los, and M.I. Katsnelson, Nat. Mater. **6**, 858 (2007).

[2] A.L. Vázquez De Parga, F. Calleja, B. Borca, M.C.G. Passeggi, J.J. Hinarejos, F. Guinea, and R. Miranda, Phys. Rev. Lett. **100**, 056807 (2008).

[3] S. Luo, G. Hao, Y. Fan, L. Kou, C. He, X. Qi, C. Tang, J. Li, K. Huang, and J. Zhong, Nanotechnology **26**, 105705 (2015).

[4] J.C. Meyer, A.K. Geim, M.I. Katsnelson, K.S. Novoselov, T.J. Booth, and S. Roth, Nature **446**, 60 (2007).

[5] W. Bao, F. Miao, Z. Chen, H. Zhang, W. Jang, and C. Dames, Nat. Nanotechnol. **4**, 562 (2009).

[6] C.-C. Chen, W. Bao, J. Theiss, C. Dames, C.N. Lau, and S.B. Cronin, Nano Lett. **9**, 4172 (2009).

[7] M.L. Ackerman, P. Kumar, M. Neek-Amal, P.M. Thibado, F.M. Peeters, and S. Singh, Phys. Rev. Lett. **117**, 126801 (2016).

[8] J. Brivio, D.T.L. Alexander, and A. Kis, Nano Lett **11**, 5148 (2011).

[9] S. V. Morozov, K.S. Novoselov, M.I. Katsnelson, F. Schedin, L.A. Ponomarenko, D. Jiang, and A.K. Geim, Phys. Rev. Lett. **97**, 016801 (2006).

[10] M.. Katsnelson and A.. Geim, Philos. Trans. R. Soc. A Math. Phys. Eng. Sci. **366**, 195 (2008).

[11] Z. Yu, L.Z. Sun, C.X. Zhang, and J.X. Zhong, Appl. Phys. Lett. **96**, 173101 (2010).

[12] Z. Guo, D. Zhang, and X.-G. Gong, Appl. Phys. Lett. **95**, 163103 (2009).

[13] L. Lindsay, D.A. Broido, and N. Mingo, Phys. Rev. B **82**, 115427 (2010).

[14] X. Li, K. Maute, M.L. Dunn, and R. Yang, Phys. Rev. B **81**, 245318 (2010).

[15] N. Wei, L. Xu, H.-Q. Wang, and J.-C. Zheng, Nanotechnology **22**, 105705 (2011).

[16] J.W. Jiang, N. Yang, B.S. Wang, and T. Rabczuk, Nano Lett. **13**, 1670 (2013).

[17] Z. Ding, Q.X. Pei, J.W. Jiang, and Y.W. Zhang, J. Phys. Chem. C **119**, 16358 (2015).

[18] L. Zhu, T. Zhang, Z. Sun, J. Li, G. Chen, and S.A. Yang, Nanotechnology **26**, 465707 (2015).

[19] A.L. Moore and L. Shi, Mater. Today **17**, 163 (2014).

[20] M.M. Sadeghi, S. Park, Y. Huang, D. Akinwande, Z. Yao, J. Murthy, and L. Shi, J. Appl. Phys. **119**, 235101 (2016).

[21] D. Akinwande, N. Petrone, and J. Hone, Nat. Commun. **5**, 5678 (2014).

[22] I. Jo, M.T. Pettes, E. Ou, W. Wu, L. Shi, I. Jo, M.T. Pettes, E. Ou, W. Wu, and L. Shi, Appl. Phys. Lett. **104**, 201902 (2014).

[23] B. Smith, B. Vermeersch, J. Carrete, E. Ou, J. Kim, N. Mingo, D. Akinwande, and L. Shi, Adv. Mater. **29**, 1603756 (2016).

[24] J. Kim, E. Ou, D.P. Sellan, and L. Shi, Rev. Sci. Instrum. **86**, 044901 (2015).

[25] E. Fleming, F. Du, E. Ou, L. Dai, and L. Shi, Carbon N. Y. **145**, 195 (2019).

[26] P. Poncharal, Z.L. Wang, D. Ugarte, W.A. De Heer, P. Poncharal, Z.L. Wang, D. Ugarte, and W.A. De Heerl, Science (80-.). **283**, 1513 (1999).

[27] M. Arroyo and T. Belytschko, Phys. Rev. Lett. **91**, 215505 (2003).

[28] I. Nikiforov, D.B. Zhang, R.D. James, and T. Dumitrič, Appl. Phys. Lett. **96**, 123107 (2010).

[29] F. Pan, G. Wang, L. Liu, Y. Chen, Z. Zhang, and X. Shi, J. Mech. Phys. Solids **122**, 340 (2019).

[30] S. Tongay, J. Suh, C. Ataca, W. Fan, A. Luce, J.S. Kang, J. Liu, C. Ko, R. Raghunathanan, J. Zhou, F. Ogletree, J. Li, J.C. Grossman, and J. Wu, Sci. Rep. **3**, 2657 (2013).

[31] S. Li, Q. Zheng, Y. Lv, X. Liu, X. Wang, P.Y. Huang, D.G. Cahill, and B. Lv, Science

(80-.). **361**, 579 (2018).

[32] J.M. Ziman, *Electrons and Phonons: The Theory of Transport Phenomena in Solids* (Oxford University Press, 1960).

[33] G.P. Srivastava, *The Physics of Phonons* (CRC press, 1990).

[34] S. Tamura, Phys. Rev. B **30**, 849 (1984).

[35] M. Omini and A. Sparavigna, Phys. Rev. B **53**, 9064 (1996).

[36] D.A. Broido, M. Malorny, G. Birner, N. Mingo, and D.A. Stewart, Appl. Phys. Lett. **91**, 231922 (2007).

[37] L. Lindsay, Nanoscale Microscale Thermophys. Eng. **20**, 67 (2016).

[38] N.A. Katcho, J. Carrete, W. Li, and N. Mingo, Phys. Rev. B **90**, 094117 (2014).

[39] C.A. Polanco and L. Lindsay, Phys. Rev. B **97**, 014303 (2018).

[40] C.A. Polanco and L. Lindsay, Phys. Rev. B **98**, 014306 (2018).